Materials Characterization 197 (2023) 112708

Contents lists available at ScienceDirect

Materials Characterization

journal homepage: www.elsevier.com/locate/matchar

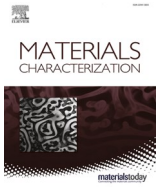

The influence of processing and texture on the grain boundary character distribution of an austenitic Ni—30Fe alloy

Hossein Beladi [a,*], Qi Chao [a,b], Vahid Tari [c], A.D. Rollett [d], Gregory S. Rohrer [d]

[a] Institute for Frontier Materials, Deakin University, Geelong, Victoria 3216, Australia
[b] School of Engineering, Deakin University, Geelong, Victoria 3216, Australia
[c] ATI Specialty Materials, Monroe, NC, 28111, USA
[d] Department of Materials Science and Engineering, Carnegie Mellon University, Pittsburgh, PA 15213-3890, USA

ARTICLE INFO

Keywords:
Casting
Iterative recrystallisation
CSL boundaries
Overall texture
Microstructure evolution mechanism

ABSTRACT

The effect of processing route (casting versus iterative recrystallisation) on the texture and grain boundary network characteristics (i.e., population, plane orientation and connectivity) of an austenitic Ni—30Fe alloy has been determined. The processing route determined the mechanism of microstructure evolution (i.e., nucleation and growth), and this influenced the overall texture and grain boundary network characteristics. In material processed by iterative recrystallisation, the microstructure was dominated by a well-connected network of $\sum 3$ and $\sum 9$ boundaries with minimum energy grain boundary plane orientations. However, in the cast material, the $\sum 3$ and $\sum 9$ boundaries had lower relative areas and were more isolated, suggesting they formed through the accidental impingement of randomly oriented nuclei during solidification. As a result, the $\sum 3$ and $\sum 9$ boundaries were less likely to be terminated on the lowest energy planes and more incoherent $\sum 3$ and $\sum 9\{\bar{2}21\}$ symmetric tilt grain boundaries were formed due to the change in the arrangement of triple junctions. In the two cast microstructures, the grain boundary misorientation angle distribution was strongly correlated with the texture. For the material with a strong θ-fibre (i.e., ⟨001⟩//ND), the misorientation angle distribution was flat and had a maximum at 45°, an expected result of limiting the grain boundary misorientations the [100] axis.

1. Introduction

One approach to enhance the performance of polycrystalline materials is to engineer the microstructure constituents based on their contributions to the property of interest. Polycrystalline materials can be thought of as composites of the grain interior regions and grain boundaries, each with characteristic properties. The grain boundary component is important because it is known that material mechanical performance cannot be specified by the grain size alone, as grain refinement does not always lead to higher strength [1]. While the grain size specifies the density and spacing of grain boundaries, it provides no information on the types of grain boundaries in the material. The atomic structure of the interface (i.e., defect density) varies with the type of grain boundary, which influences certain properties of materials (e.g., diffusion and strength). Hence, the types of boundaries in the three-dimensional grain boundary network, and their connectivity, can contribute to realizing the desired material property. This approach is known as grain boundary engineering (GBE), which requires knowledge of the parameters affecting the grain boundary network during microstructure evolution.

Since the introduction of the GBE concept in mid-1980 [2], there have been significant advances in manipulating the grain boundary network in materials with diverse crystal structures through various approaches, namely iterative recrystallisation [3], modification of alloy composition [3–5], controlling the phase transformation mechanism (i.e., shear vs diffusion) [4,6,7], controlling variant selection [4,5,8] and texture [7,9–12]. These GBE approaches exploit different microstructure evolution mechanisms, namely recrystallisation and phase transformation, depending on the alloy composition and processing route.

Polycrystalline materials are processed to enhance the property of interest for the required applications. The microstructure evolution taking place during processing may lead to distinct preferred crystallographic texture, which influences the distribution of grain boundaries and the way that they are connected. For example, if a material has a texture that aligns crystals along a certain axis, then the grain boundary misorientations are constrained to be around that common axis.

* Corresponding author.
E-mail address: hossein.beladi@deakin.edu.au (H. Beladi).

https://doi.org/10.1016/j.matchar.2023.112708
Received 29 November 2022; Received in revised form 11 January 2023; Accepted 30 January 2023
Available online 2 February 2023

However, the relative influence of the microstructure evolution mechanism and the texture on the population of different types of boundaries and the way they are connected is currently not clear. The present study aims to address this question by comparing the grain boundary network characteristics of three austenitic Ni—30Fe alloy microstructures produced in different ways. One is produced by iterative recrystallisation, one by casting in a mould, and one by directional solidification into a columnar structure. In each case, the microstructure was characterised using electron backscatter diffraction (EBSD) based orientation mapping and the stereological interpretation of this data using the five-parameter characterisation approach [13]. The texture, misorientation angle distributions, grain boundary plane distributions, and triple junction distributions are compared and interpreted based on the mechanism of microstructure evolution, which leads to very different grain boundary network characteristics.

2. Experimental procedure

The fully austenitic material was received as a 40 mm thick billet, having Ni-29.5Fe-0.01C-0.02Mn (in wt%) composition, hereafter called Ni—30Fe alloy. The billet thickness was initially decreased to ~20 mm by conducting several rolling passes in the 1200–1000 °C temperature range. Then, the hot rolled material was processed using one of the three following routes.

2.1. Iterative recrystallisation thermomechanical processing

A solid torsion sample was machined from the hot rolled material, having 6.7 mm diameter and 20 mm gauge length. The solid torsion sample was subjected to an iterative recrystallisation processing routine utilising a torsion rig, which illustrated in ref. [14]. The thermomechanical schedule initially involved reheating the sample to 1200 °C and isothermally holding for 80 s to avoid any temperature gradient throughout the gauge length of sample. Afterwards, two torsion deformation passes were applied using a 0.4 strain at a true strain rate of 1 s^{-1}. Each torsion deformation pass was followed by an isothermal holding time of 40 s, which leads to fully recrystallised microstructure [15]. Subsequently, the specimen was cooled at 2 °C/s to 1000 °C and isothermally held for 120 s. The sample was then subjected to 0.3 strain at a true strain rate of 1 s^{-1}, held isothermally for 150 s and then immediately water-quenched. This resulted an equiaxed grain structure with an average size of ~27 ± 1 μm.

2.2. Mould casting process

A cast material was produced by melting a piece of hot rolled Ni—30Fe alloy in a ceramic crucible under argon gas. Afterwards, the melt was transferred to a mould with a dimension of 10 mm × 10 mm × 80 mm and solidified under argon gas, which led to very coarse equiaxed grains with an average size of ~750 ± 30 μm.

2.3. Columnar casting process

Hot rolled material was melted using an arc melting furnace (Arc 50) and then solidified within a water-cooled copper mould with a dimension of 40 mm × 15 mm × 10 mm. The welding power was set at 280 A current using a tungsten arc electrode. The sample was then flipped within the water-cooled copper mould and underwent five remelting and solidification processes to minimise the composition gradient throughout the sample. This process leads to the formation of columnar grain morphology because of the strong temperature gradient.

The microstructures produced through the three different processing routes were characterised by EBSD. For the solid torsion sample, the microstructure was examined on a tangential section plane ~100 μm in depth beneath the gauge length surface. For both cast conditions, multiple samples were prepared for EBSD measurements from different ingot locations to assure that the result represents the overall microstructure characteristics throughout the ingot. EBSD data was collected on two perpendicular cross sections to minimise the texture bias for grain boundary plane characterisation and/or reveal the grain morphology. The EBSD specimens were prepared using standard mechanical grinding and polishing procedures, followed by a colloidal silica slurry polish. Multiple EBSD maps were acquired for each processing route using a FEI Quanta 3D FEG SEM/FIB instrument, operating at 20 kV and 8 nA current. The EBSD map parameters are summarised in Table 1 for all processing routes. The average confidence index of EBSD maps varied between 0.70 and 0.85, depending on step size and microstructure characteristics (i.e., processing route condition).

The TexSEM Laboratories (TSL) software was used to perform both EBSD data acquisition and post-processing. Several EBSD data post-processing functions in TSL software were employed to extract boundary lines/traces for computing the grain boundary character distribution using an automated stereological approach [13]. Ambiguous data were initially eliminated through a grain dilation clean-up function. Then, a single orientation was designated to every grain by averaging all orientations within a grain. The reconstruct grain boundary function in the TSL software was employed to approximate the grain boundary traces/lines through straight line segments using the smoothing process. In the current study, at least 50,000 boundary line segments were acquired for each processing route (Table 1) to reliably analyse the grain boundary plane character distribution with 10° resolution using the five-parameter characterisation approach [13]. $\sum 3$ and $\sum 9$ boundaries were defined using angular deviations of 8.66° and 5°, respectively, from the corresponding ideal lattice misorientation based on the Brandon criterion [16]. The overall texture was plotted using the Atex post-processing software [17]. The statistical error was computed using the standard error $= \frac{S}{\sqrt{N}}$, where S and N are standard deviation and number of measurements, respectively. Misorientation angles >15° were classified as high-angle grain boundaries to measure the grain size.

3. Results and discussion

The sample produced through iterative recrystallisation displayed equiaxed grains having a size of 27 ± 1 μm on average (Fig. 1a). A prominent peak was observed in the misorientation angle distribution at the position of 60°, corresponding misorientation axes strongly centred at the ⟨111⟩ direction (Fig. 2a). This manifests a high concentration of first-order $\sum 3$ twin boundaries, described by the 60°/⟨111⟩ misorientation. In other words, 52.6 ± 0.1% of the total high-angle grain boundary length can be assigned to $\sum 3$ twin boundaries, as frequently appeared in the microstructure (Fig. 1a, Table 2). The formation of $\sum 3$ twin boundaries during recrystallisation can be attributed to the growth accident mechanism, a model that has been shown to successfully predict different annealing twin morphologies [18]. This model suggests that the annealing twins initiate on {111} propagating steps, which exist on the moving grain boundary. This promotes the formation of Shockley partials in the vicinity of boundary, repelling each other to form a twin as they glide away from the boundary [18].

A slight peak also appeared at ~39° where misorientation axes are clustered about the ⟨101⟩ direction (Fig. 2a). This suggests the presence

Table 1
The EBSD condition for different processing routes.

Condition	Step size	Area	Number of boundary segments
Iterative recrystallisation	1 μm	1280 μm × 640 μm × 8	~ 60,000
Mould casting	10 μm	3200 μm × 3000 μm × 189	~ 52,000
Columnar casting	10 μm	3200 μm × 3000 μm × 157	~ 51,000

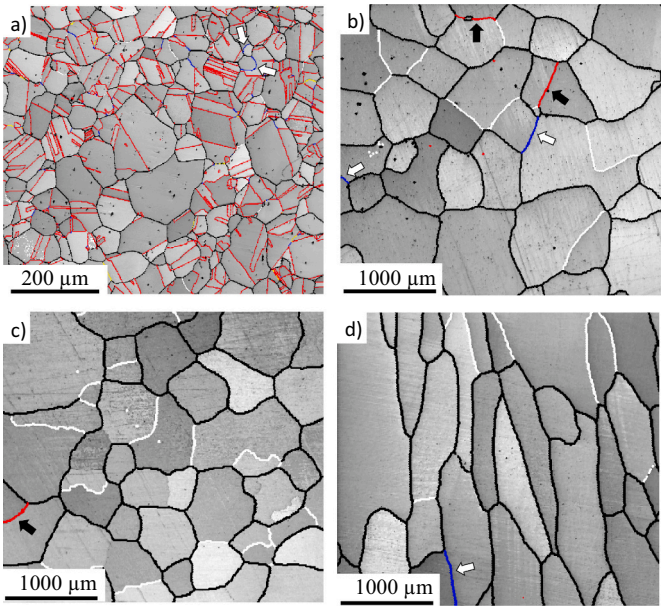

Fig. 1. The microstructure of Ni—30Fe alloy subjected to different processing routes: a) iterative recrystallisation, b) mould casting, and c) and d) represent arc melting casting at side view and top view cross-sections, respectively. White, black, red, blue and yellow lines are low-angle (i.e., $\theta < 15°$), high-angle (i.e., $\theta \geq 15°$), Σ3, Σ9 and Σ27 boundaries, respectively. Black and white arrows represent isolated Σ3 and Σ9 boundaries, respectively. (For interpretation of the references to colour in this figure legend, the reader is referred to the web version of this article.)

of second-order ∑9 twin boundaries, defined by the 39°/⟨101⟩ misorientation. The ∑9 twin boundaries had a length fraction of ~3.5 ± 0.3% and are usually connected to ∑3 boundaries (Fig. 1a), making up 5.9 ± 0.1% of triple junctions (Table 3). This arrangement is expected from the coincidence lattice site (CSL) boundary multiplication rules, where the impingement of two ∑3 s leads to the formation of a ∑9 at the corresponding triple junction (i.e., ∑3 + ∑3 → ∑9) [19]. However, in some cases, ∑9 boundaries were either isolated (~ 1.46 ± 0.1%) or only connected to one ∑3 boundary (0.6 ± 0.01%, Table 3 and Fig. 1a). ∑27 (31.6°/[110]) boundary was also observed in the microstructure (Fig. 1a), largely appeared where ∑3 and ∑9 boundaries impinge (i.e., ∑3 + ∑9 → ∑27). In general, the misorientation angle distribution is typical for materials with low-medium stacking fault energy, where the iterative static recrystallisation promotes the presence of high fraction of ∑3 and ∑9 boundaries through the twinning multiplication phenomenon [19]. This process ultimately weakens the overall texture, as it frequently alters the grain orientations throughout the microstructure, randomising the texture. This is consistent with the current result where the overall texture is relatively weak with a strength of 1.92 multiples of a random distribution (MRD) (Fig. 3a).

Mould casting led to a very coarse equiaxed grain structure having an approximate average size of ~750 ± 30 μm (Fig. 1b). The corresponding misorientation angle distribution was similar to the random distribution where the maximum appears at 45° misorientation angle [20] (Fig. 2b). This is closely reflected in the overall texture, showing a relatively weak

Table 2
Length fractions of coherent and incoherent ∑3 boundaries of Ni—30Fe alloy produced through different processing routines, considering a deviation angle of 10° from (111) plane.

Processing route	Length fraction		
	Coherent ∑3 (%)	Incoherent ∑3 (%)	Total ∑3*
Iterative recrystallisation	45.2 ± 0.2	7.4 ± 0.1	52.6 ± 0.1
Mould casting	0.99 ± 0.02	3.68 ± 0.05	4.67 ± 0.07
Columnar casting	0.11 ± 0.01	0.33 ± 0.01	0.44 ± 0.01

* ∑3 boundary was defined using angular deviations of 8.66°, from the corresponding ideal lattice misorientation based on the Brandon criterion [16].

Table 3
Triple junction classification based on different types of boundaries, namely coherent ∑3 and incoherent ∑3, ∑9 and random (R) boundaries for Ni-30 alloy produced through different processing routes. Coherent ∑3 and incoherent ∑3 were differentiated considering 10° deviation angle from (111) plane.

Triple junction classification	Processing routes		
	Iterative recrystallisation	Mould casting	Columnar casting
R-R-R	21.9 ± 0.5	80.6 ± 0.8	93.6 ± 0.4
Coherent ∑3-R-R	44.7 ± 0.9	3.1 ± 0.3	0.5 ± 0.1
Incoherent ∑3-R-R	10.8 ± 0.3	9.8 ± 0.7	2.1 ± 0.3
Coherent ∑3-coherent ∑3-∑9	3.6 ± 0.2	–	–
Incoherent ∑3-incoherent ∑3-∑9	1.5 ± 0.1	–	0.08 ± 0.05
Coherent ∑3-incoherent ∑3- ∑9	0.8 ± 0.1	0.03 ± 0.01	0.03 ± 0.01
Coherent ∑3-incoherent ∑3-R	0.24 ± 0.02	0.3 ± 0.1	0.03 ± 0.01
Coherent ∑3-coherent ∑3-R	0.1 ± 0.02	0.1 ± 0.05	0.01 ± 0.01
Incoherent ∑3-incoherent ∑3-R	0.05 ± 0.01	0.48 ± 0.1	0.01 ± 0.01
∑9-R-R	1.46 ± 0.1	1.3 ± 0.1	0.9 ± 0.1
Incoherent ∑3-∑9-R	0.36 ± 0.01	0.11 ± 0.05	0.01 ± 0.01
Coherent ∑3-∑9-R	0.24 ± 0.01	0.05 ± 0.03	–
Others	14.25 ± 0.3	4.13 ± 0.2	2.73 ± 0.2

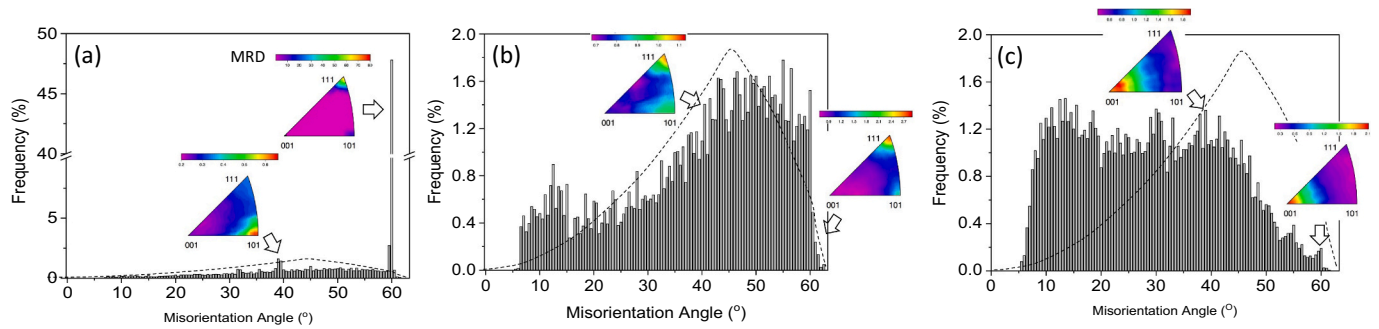

Fig. 2. Misorientation angle distribution along with the distribution of axes at rotation angle of 60°and 39° in a standard stereographic triangle for Ni—30Fe alloy subjected to different processing routes: a) iterative recrystallisation, b) mould casting and c) columnar casting. The dash line represents the random distribution.

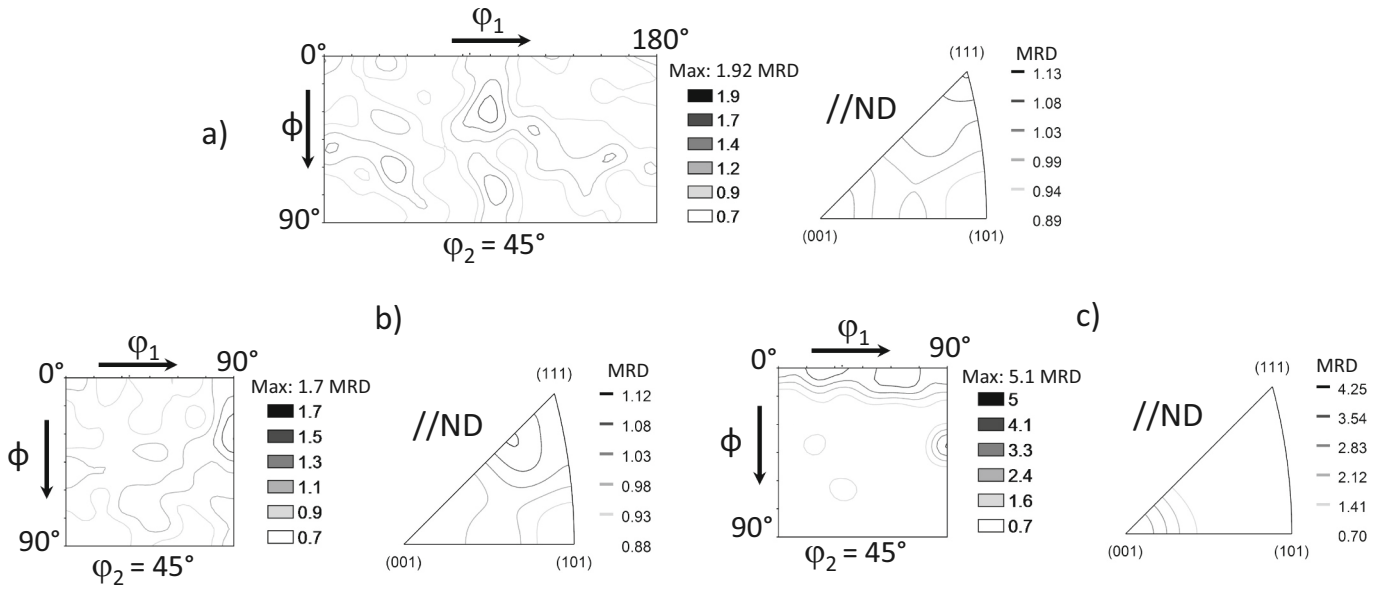

Fig. 3. The overall texture of Ni—30Fe alloy produced through different processing routes: a) iterative recrystallisation, b) mould casting and c) columnar casting. ND is normal direction. The overall textures were plotted using Atex post-processing software [17].

texture with a strength of 1.7 MRD (Fig. 3b). However, the misorientation angle distribution slightly differed from random distribution at misorientation angle ranges of <10° and 50–55° (Fig. 2b). This is not surprising as the overall texture to some extent deviated from the ideal random texture (Fig. 3b). The misorientation axes at 60° revealed a relatively weak maximum (2.8 MRD) centred at the <111> direction (Fig. 2b). This is closely reflected in the microstructure as the length fraction of ∑3 boundaries was 4.67 ± 0.07% (Fig. 1b, Table 2). This is significantly less than what was observed in the iterative recrystallisation condition (52.6 ± 0.1%, Table 2). At 39°, the misorientation axes displayed two peaks at <111> and ⟨101⟩, suggesting the presence of two distinct lattice misorientations, 39°/<111 > and 39°/<101>. The latter represents ∑9 boundary, which was measured to be <1%. Interestingly, the ∑3 and ∑9 boundaries were mostly appeared isolated and rarely connect at the triple junctions in the section plane (Fig. 1b, Table 3). This implies that ∑3 and ∑9 boundaries are not formed through the multiple twinning process, as observed in the iterative recrystallisation condition, rather their existence is accidental. This is not surprising as the nucleation of grains with random orientations occurs from the chilled surface of mould at an early stage of solidification. During the solidification, the microstructure evolves through the growth of randomly oriented nuclei at the expense of liquid, which is restricted through the impingement with other growing grain/s. Therefore, the impingement of randomly oriented grains may, theoretically, lead to any lattice misorientation as defined by random distribution [20]. In addition, one of the prerequisites of annealing twin formation is the presence of stacking fault (SF) in the vicinity of moving boundary [18]. Stacking faults can only be formed in the crystalline phase and promoted through plastic deformation, as frequently observed during the process of recrystallisation of metals with low-to-medium SF energy. During the solidification, the solid moving front however progresses in the liquid phase, which is not crystalline and does not provide a source of stacking faults. Therefore, the lack of SFs in the liquid phase in front of moving boundary impedes the formation of annealing twins. This ultimately results in the formation of a small fraction of isolated CSL boundaries despite having a relatively weak texture similar to that of the iterative recrystallisation case, where the CSL boundaries dominates the grain boundary network (Figs. 1a-b, 2a-b and 3a-b). This demonstrates that the nucleation and growth mechanisms during the material processing significantly influence the population of grain boundaries developed within the microstructure.

The microstructure that resulted from columnar casting displayed coarse elongated grains having an approximate average size of ~430 ± 20 μm, considering the cross-section plane perpendicular to the solidification/growth direction (Figs. 1c-d). The misorientation angle distribution was significantly different from other distributions, showing a relatively flat distribution in a misorientation angle range of 10–45°, beyond which the population progressively declined as it approaches 62.8° (Fig. 2c). Interestingly, the misorientation axes at 39° and 60° were both clustered about [001]. This indicates that the boundaries at these misorientation angles were not ∑3 and ∑9 boundaries. This is consistent with the results that the length fraction of these boundaries was ~0.5% (Table 2). This was also reflected in the microstructure, as they were rarely observed, and mostly appeared in a form of isolated CSL boundaries. A recent study demonstrated that a ∑9 boundary decomposes to a combination of {112} incoherent ∑3 and {111} coherent ∑3 boundaries during directional solidification of polycrystalline silicon [21]. The ∑3-∑3-∑9 boundaries arrangement at the triple junction was occasionally observed in both mould casting and columnar casting conditions (Fig. 4). However, the trace analysis revealed that these ∑3 boundaries were largely terminated at diverse plane orientations rather than ideal {111} planes. Therefore, the presence of ∑3 and ∑9 boundaries is coincidental as in the mould casting, and they did not develop through the multiple twinning process phenomenon. The columnar grained microstructure is formed through the dendritic growth process when the liquid is supercooled [22]. This is, indeed, a result of the preferred directional growth of randomly oriented nuclei, formed adjacent to the mould wall, along the heat flux direction. For materials with the face centred cubic (FCC) crystal structure, the growth of nuclei commonly takes place in the <001> direction, parallel to the axis of a pyramid having four {111} close packed planes [23]. During the growth process, dendrite stems that most closely align with the maximum heat flux direction are most favoured to grow, generating a columnar grained microstructure with <001> – fibre texture [23]. This is consistent with the current result, where a relatively strong overall θ-fibre (<001>//ND) texture (5.1 MRD), was observed (Fig. 3c).

The overall texture influences the grain boundary population in polycrystalline materials [7,9–12]. In this case, the θ-fibre promoted the formation of roughly equal numbers of boundaries misoriented about the common [001] axis up to a maximum of 45°. Because most grains

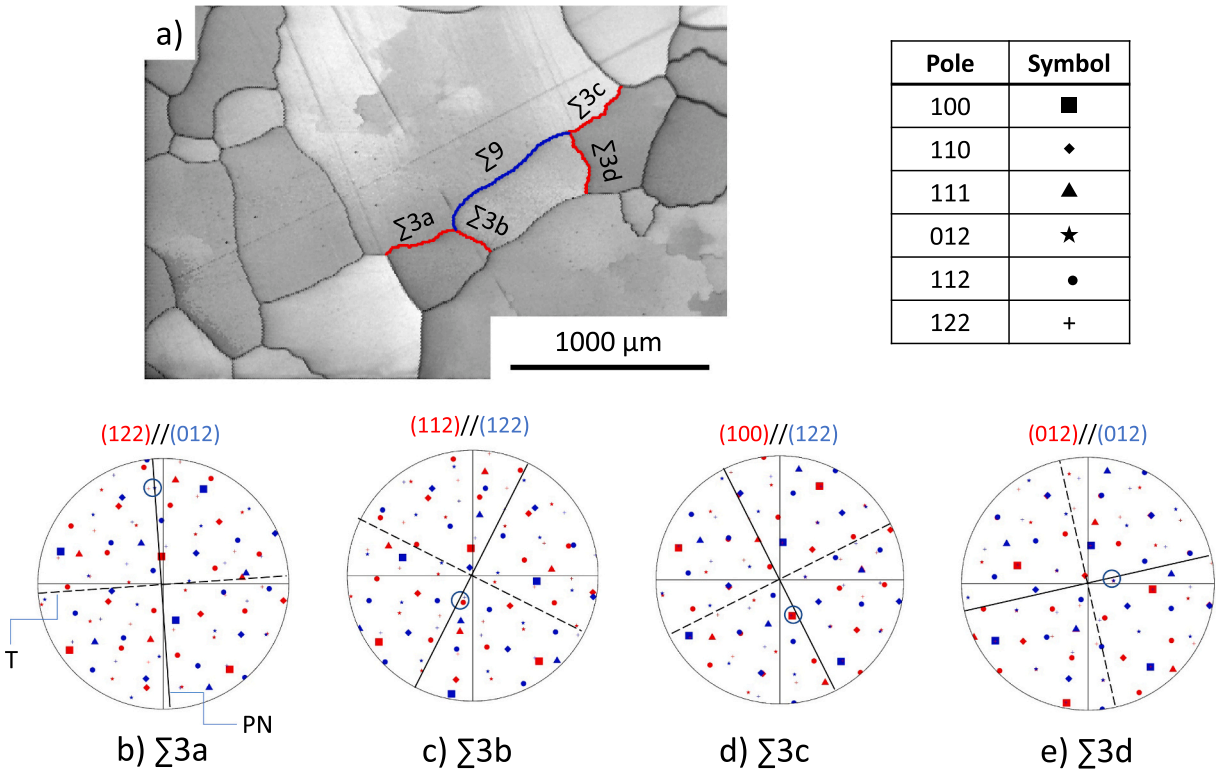

Fig. 4. a) EBSD of microstructure at top view cross-section of arc melting casting. b, c, d, e) trace analysis of Σ3 boundaries highlighted in (a). Red and blue lines in (a) are Σ3 and Σ9 boundaries, respectively. T and PN in (b) represent grain boundary trace and plane normal, respectively. (For interpretation of the references to colour in this figure legend, the reader is referred to the web version of this article.)

shared a common [001] axis, it was not possible to form ∑3 and ∑9 boundaries, which have misorientations about the [111] and [110] axes. A numerical calculation was recently used to show that for a sample with a strong [111] fibre texture, the expected distribution of misorientations was flat in the range of distinguishable misorientations about [111], which is 0 to 60° [12]. The same calculation was repeated here for the case of a [001] fibre texture (see ref. [12]) and an analogous result was obtained: a flat misorientation distribution in the range of 0 to 45°, as illustrated in Fig. 5.

This numerical calculation closely matches the misorientation angle distribution for the microstructure with strong θ-fibre texture, i.e., displaying almost flat distribution of misorientation angle up to 45° (Fig. 5). The observed distribution differs in two ways from the ideal flat distribution. First, no boundaries are observed at very low angles

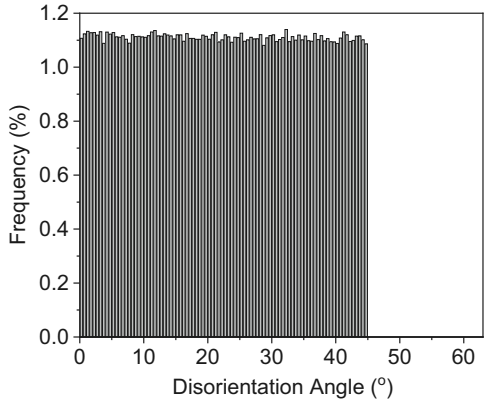

Fig. 5. The disorientation angle distribution resulted form impingement of each of pair of 1000 orientations arbitrarily selected along the θ-fibre, ignoring sample symmetry (i.e., ϕ_1 = 0–360°φ = 0°ϕ_2 = 45°).

because of the 5° threshold used to define grains in the EBSD data. Second, the experimental distribution contains some boundaries with misorientation angles >45°. These boundaries arise because of the spread of the experimental texture from the ideal θ-fibre texture that was assumed in the calculation. A similar result was reported by others, where the presence of <001> − fibre texture in columnar grained structure leads to nearly flat misorientation angle distribution and no boundaries with misorientation angles greater than ~48° [10]. The presence of low angle boundaries was explained by the formation of clusters of grains that impinged during solidification and were separated by low angle boundaries. The cluster size was shown to increase with the strength of the <001> − fibre through the simulation, leading to higher fraction of low angle boundaries [10]. This is consistent with the current calculation, suggesting that the probability of formation of any misorientation angle up to 45° becomes equal, when the microstructure has prefect <001> − fibre texture (Fig. 5).

The nucleation mechanism that operates during the columnar casting process is similar to mould casting process, although the growth of randomly oriented nuclei is largely controlled by the heat flux for the former, significantly altering the grain morphology and overall texture (Figs. 1b-d and 3b-c). When we compare these two results, we see that when the microstructure formation mechanism is essentially the same (nucleation and growth) it is the texture that has the dominant influence on the grain boundary distribution.

The relative areas of grain boundary planes for all boundaries, plotted in the crystal reference frame, displayed a very high anisotropy with a peak appearing at the (111) orientation having ~6.8 MRD for the iterative recrystallisation condition (Fig. 6a). This indicates that the area of (111) plane was ~580% larger than anticipated for a random distribution. The intensity of (001) orientation was minimum (i.e., ~ 0.4 MRD) and the (101) orientation had an intensity of ~2 MRD (Fig. 6a). This observation is well aligned with the idea that {111} planes, representing close packed plane in FCC materials with relatively low

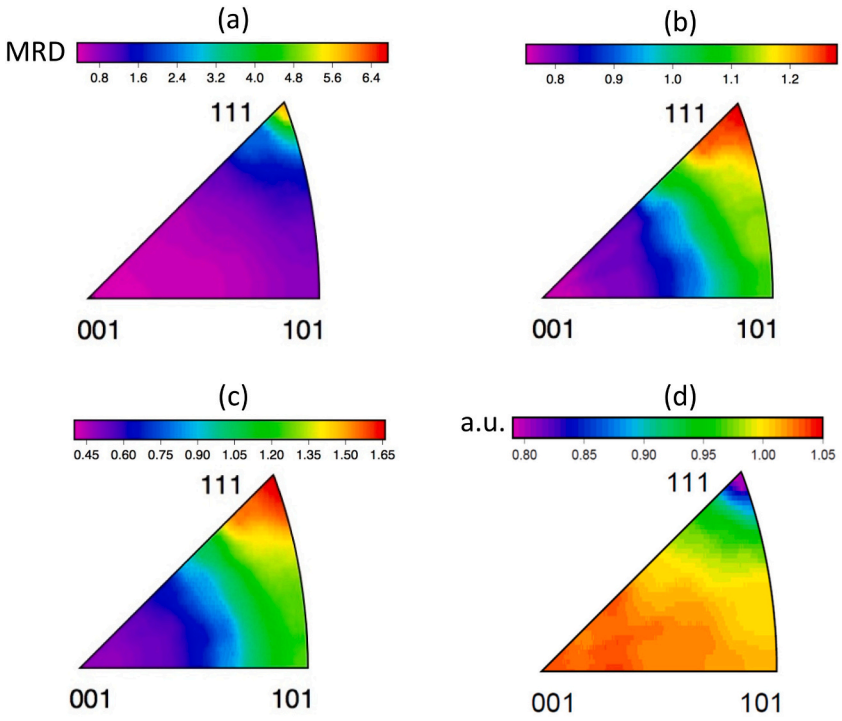

Fig. 6. The relative area of grain boundary planes distribution for all boundaries, ignoring misorientation: a) iterative recrystallization, b) mould casting and (c) columnar casting. d) the distribution of grain boundary energy of commercially pure Ni adopted from [24]. MRD and a.u. represent multiples of a random distribution and arbitrary unit, respectively.

boundary energies (Fig. 6d), which ultimately leads to the enhancement of their population in the microstructure [24,25].

The distribution is qualitatively similar for mould casting and columnar casting conditions, showing a maximum at the position of the {111} grain boundary plane. However, the intensity was significantly reduced, exhibiting ~1.3 MRD and ~ 1.66 MRD for mould and columnar casting conditions, respectively (Figs. 6 b,c). This is not surprising as the population of $\sum 3$ boundaries is significantly smaller in

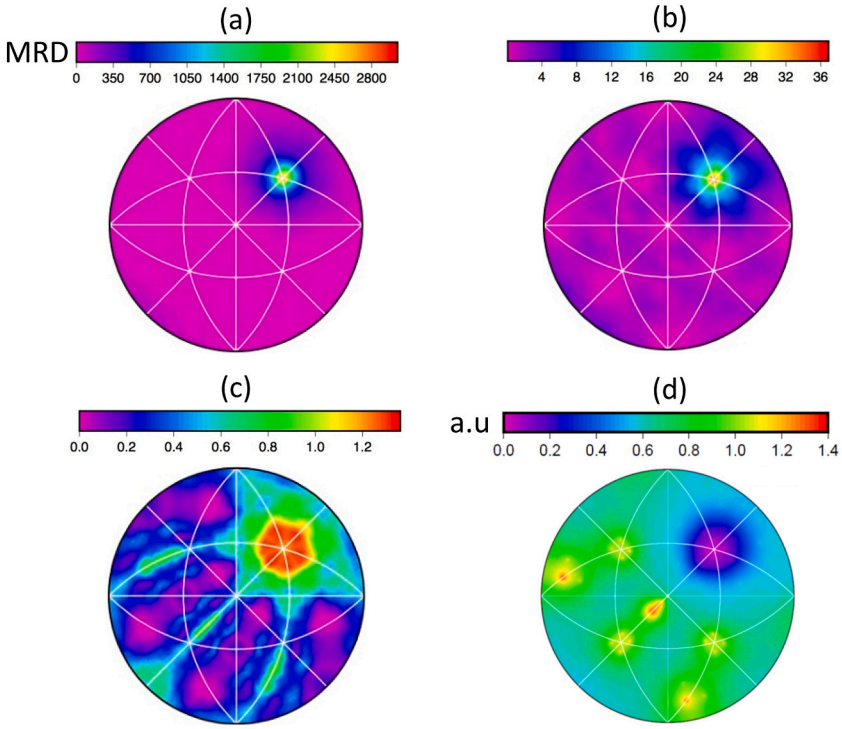

Fig. 7. (a-c) the distribution of plane normals for $\Sigma 3 = 60°/[111]$ boundaries in Ni-30 alloy produced through different processing routes: a) iterative recrystallization, b) mould casting and c) columnar casting. d) the grain boundary energy distribution for $\Sigma 3$ boundaries measured for commercial pure Ni adopted from [24]. MRD and a.u. represent multiples of a random distribution and arbitrary unit, respectively.

both casting conditions compared with the iterative recrystallisation sample (Table 2).

The grain boundary plane distribution of ∑3 displayed a maximum at the (111)//(111) orientation, representing a twist character for all processing routes (Figs. 7a-c). This is consistent with the position of the minimum energy orientation measured and calculated for ∑3 boundary in FCC materials [24–27], as shown in Fig. 7d, displaying the energy distribution measured for a commercially pure Ni. However, the intensity of maxima is significantly higher for the iterative recrystallisation condition (i.e., ~ 3000 MRD) in comparison with mould casting and columnar casting, displaying ~37 MRD and ~ 1.3 MRD, respectively (Figs. 7a-c). The significant drop in the (111) intensity is closely related to the microstructure characteristics of cast products, which have few ∑3 boundaries (Table 2). Interestingly, the ∑3 boundary planes still exhibited a mild bias towards the (111) position despite being formed by accident upon casting. However, it should be emphasized that they were largely characterised as incoherent ∑3 boundaries, i.e., mostly deviating from the low energy {111} plane orientation arrangement (Table 2).

The three different processing routes led to a significant change in the grain boundary plane distribution of ∑9. While the maxima were along their [110] zone for all processing conditions (Figs. 8a-d), the orientation of the maximum differed, spanning a range of symmetric and asymmetric tilt characters. For the iterative recrystallisation route, the main maxima was observed at $(1\bar{1}4)//(1\bar{1}4)$ symmetrical tilt position, extending towards $(001)//(1\bar{1}\bar{2})$ and $(1\bar{1}1)//(\bar{1}1\bar{5})$ planes (Fig. 8a). The presence of these local maxima is qualitatively consistent with previously reported observations [15,24,25,28–31], and closely correlated with the positions of minimum energy calculated for pure Ni (Fig. 8e) [32]. The position of maxima significantly altered for mould casting, appearing at the $(\bar{2}21)//(\bar{2}21)$ symmetric tilt position; calculations have shown that this symmetric tilt grain boundary (STGB) has a larger energy than the $(1\bar{1}4)//(1\bar{1}4)$ STGB (Figs. 8b,d,e). For the columnar condition, the ∑9 distribution displayed multiple peaks spread along the zone of [110] tilt boundaries (Fig. 8c).

For microstructures with many ∑3 boundaries, the ∑9 boundary occurs mainly as a geometrically required element that forms as a result of the impingement of two ∑3 s at the triple junction. Therefore, the ∑9 grain boundary plane is geometrically confined by the characteristics of the ∑3 boundary at the triple junction, as recently demonstrated by the current authors [31]. It was clearly shown that the intersection of two perfect coherent ∑3 boundaries promotes the formation of the $(1\bar{1}4)//(1\bar{1}4)$ symmetric tilt ∑9 boundary, having the lowest energy configuration [32–34]. However, the ∑9 can adopt any symmetric/asymmetric plane orientations along the zone of [110] tilt boundaries as the ∑3 s at the corresponding triple junction deviate from ideal coherency [31]. This is consistent with the current result as the ∑9 boundaries during casting were isolated and did not form via the multiple twinning phenomenon (Figs. 1b-d). In other words, they are mostly connected to random boundaries at the triple junctions rather than coherent ∑3 boundaries (Table 3). Therefore, the maxima in their grain boundary plane distributions did not follow the minimum energy arrangement. This is more obvious for mould casting condition, forming a peak at $(\bar{2}21)//(\bar{2}21)$ STGB with a relatively higher energy (Figs. 8b,d, e). The current result suggests that the processing route can significantly affect the grain boundary plane orientation for a specific type of grain boundary (e.g., ∑9) by altering the types of triple junctions they are attached to. In other words, these changes are imposed by the distinct nucleation and growth mechanisms taking place during microstructure evolution, which in turn change the arrangement of triple junctions and subsequently the grain boundary plane orientation/s.

4. Conclusion

An austenitic Ni—30Fe alloy was processed by three routes (two casting methods and iterative recrystallisation) to evaluate the influence of microstructure evolution (i.e., nucleation and growth) and overall texture on the grain boundary network characteristics. The findings are summarised as follows:

1) the processing route changed the mechanism of microstructure evolution, and this affected the overall texture and grain boundary network characteristics.

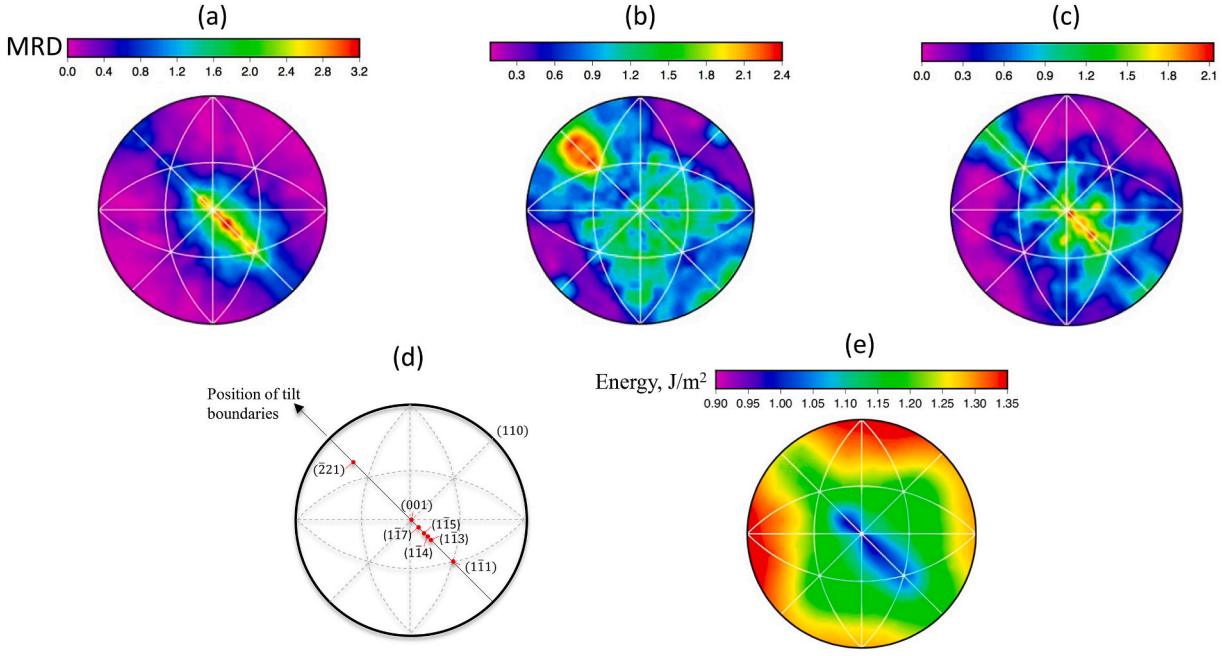

Fig. 8. (a-c) the distribution of plane normals for Σ9 = 39°/[110] boundaries in Ni-30 alloy produced through different processing routes: a) iterative recrystallization, b) mould casting and c) columnar casting. d) schematic representation of plane orientations positions for [110] tilt boundaries. e) the grain boundary energy distribution for Σ9 boundaries computed for Ni adopted from [32]. MRD represents multiples of a random distribution.

2) the materials processed by iterative recrystallisation and casting into a mould had similar near random texture, but very different grain boundary distributions, illustrating a case where the mechanism of microstructure evolution had the most influence on the grain boundary network.
3) The iterative recrystallisation process promoted the formation of $\sum 3$ and $\sum 9$ boundaries with minimum energy plane orientations through the multiple twinning process.
4) During the casting process, $\sum 3$ and $\sum 9$ boundaries had a low population and were unlikely to be connected to other $\sum 3$ and $\sum 9$ boundaries. The boundaries formed through the impingement of randomly oriented nuclei. As a result, the CSL boundaries were not necessarily terminated at plane/s with low energy arrangement (e.g., incoherent $\sum 3$ and/or $\sum 9$ with $\{\bar{2}21\}$ orientation) because of the change in their triple junction arrangements.
5) The microstructure evolution mechanism of the two cast materials was essentially the same, but they had very different textures, and this greatly altered the distribution of grain boundary misorientation angles. The observation of an approximately constant misorientation angle distribution until 45° was consistent with a numerical calculation of the misorientation distribution expected for a material with an ideal θ-fibre texture (i.e., <001>//ND).

Declaration of Competing Interest

The authors declare that they have no known competing financial interests or personal relationships that could have appeared to influence the work reported in this paper.

Data availability

The raw/processed data required to reproduce these findings cannot be shared at this time as the data also forms part of an ongoing study.

Acknowledgements

Dr. Murugesan Annasamy is acknowledged for the casting of the Ni—30Fe alloy. Deakin University's Advanced Characterisation Facility is acknowledged for use of the EBSD instruments. ADR acknowledges partial support from the National Science Foundation under grant number DMR-1905910.

References

[1] T.P. Weihs, V. Zinoviev, D.V. Viens, E.M. Schulson, The strength, hardness and ductility of Ni_3Al with and without boron, Acta Metall. 35 (1987) 1109–1118.
[2] T. Watanabe, Grain boundary design for new materials, Trans. Japan Inst. Metals 27 (1986) 73–82.
[3] V. Randle, Mechanism of twinning-induced grain boundary engineering in low stacking-fault energy materials, Acta Mater. 47 (1999) 4187.
[4] E. Farabi, V. Tari, P.D. Hodgson, G.S. Rohrer, H. Beladi, On the grain boundary network in a Ti-6Al-4V martensite, J. Mater. Sci. 55 (2020) 15299–15321.
[5] V. Govindaraj, E. Farabi, S. Kada, P.D. Hodgson, R. Singh, G.S. Rohrer, H. Beladi, Effect of manganese on the grain boundary network of lath martensite in maraging stainless steels, J. Alloys Compd. 886 (2021), 161333.
[6] H. Beladi, G.S. Rohrer, A.D. Rollett, V. Tari, P.D. Hodgson, The distribution of intervariant crystallographic planes in a lath martensite using five macroscopic parameters, Acta Mater. 63 (2014) 86–98.
[7] H. Beladi, G.S. Rohrer, The role of thermomechanical routes on the distribution of grain boundary and interface plane orientations in transformed microstructures, Metall. Mater. Trans. A 48 (2017) 2781–2790.
[8] A. Mirzaei, R. Ghaderi, P.D. Hodgson, X. Ma, G.S. Rohrer, H. Beladi, The influence of parent austenite characteristics on the intervariant boundary network in a lath martensitic steel, J. Mater. Sci. 57 (2022) 8904–8923.
[9] H. Beladi, E. Farabi, P.D. Hodgson, M.R. Barnett, G.S. Rohrer, D. Fabijanic, Microstructure evolution 316L stainless steel using solid-state additive friction stir deposition, Philos. Mag. 102 (2022) 618–633.
[10] D.A. West, B.L. Adams, Analysis of orientation clustering in a directionally solidified nickel-based ingot, Metall. Mater. Trans. A 28 (1997) 229–236.
[11] R.E. Garcia, M.D. Vaudin, Correlations between the crystallographic texture and grain boundary character in polycrystalline materials, Acta Mater. 55 (2007) 5728–5735.
[12] H. Beladi, V. Tari, A.D. Rollett, G.S. Rohrer, The influence of γ-fibre texture on grain boundary character distribution of an IF-steel, Scr. Mater. 222 (2023), 115042.
[13] G.S. Rohrer, D.M. Saylor, B.E. Dasher, B.L. Adams, A.D. Rollett, P. Wynblatt, The distribution of internal interfaces in polycrystals, Z. Met. 95 (2004) 197–214.
[14] H. Beladi, G.L. Kelly, P.D. Hodgson, The effect of multiple deformations on the formation of ultrafine grained steels, Metall. Mater. Trans. A 38 (2007) 450–463.
[15] H. Beladi, P. Cizek, A.S. Taylor, G.S. Rohrer, P.D. Hodgson, Static softening in a Ni-30Fe austenitic model alloy after hot deformation: microstructure and texture evolution, Metall. Mater. Trans. A 48 (2017) 855–867.
[16] D.G. Brandon, The structure of high-angle grain boundaries, Acta Metall. 14 (1966) 1479–1484.
[17] B. Beausir, J.-J. Fundenberger, Analysis Tools for electron and X-Ray Diffraction, ATEX - Software. www.atex-software.eu.
[18] S. Mahajan, C.S. Pande, M.A. Imam, B.B. Rath, Formation of annealing twins in fcc crystals, Acta Mater. 45 (1997) 2633–2638.
[19] K. Miyazawa, Y. Iwasaki, K. Ito, Y. Ishida, Combination rule of sigma values at triple junctions in cubic polycrystals, Acta Crystallogr. 52 (1996) 787–796.
[20] J.K. MacKenzie, Second paper on statistics associated with the random disorientation of cubes, Biometrika 45 (1958) 229–240.
[21] L.-C. Chuang, K. Maeda, K. Shiga, H. Morito, K. Fujiwara, A {112}$\sum 3$ grain boundary generated from decomposition of a $\sum 9$ grain boundary in multicrystalline silicon during directional solidification, Scr. Mater. 167 (2019) 46–50.
[22] W. Kurz, D.J. Fisher, Fundamentals of Solidification, Trans Tech, Publications Aedermannsdorf, Switzerland, 1989, pp. 49–50 and 53–58.
[23] F. Weinberg, B. Chalmers, Further observations on dendritic growth in metals, Can. J. Phys. 30 (1952) 488–502.
[24] J. Li, S.J. Dillon, G.S. Rohrer, Relative grain boundary area and energy distributions in nickel, Acta Mater. 57 (2009) 4304–4311.
[25] H. Beladi, N.T. Nuhfer, G.S. Rohrer, The five parameter grain boundary character and energy distributions in a fully austenitic high manganese steel using three dimensional data, Acta Mater. 70 (2014) 281–289.
[26] E.A. Holm, D.L. Olmsted, S.M. Foiles, Comparing grain boundary energies in face-centered cubic metals: Al, au, cu and Ni, Scr. Mater. 63 (2010) 905–908.
[27] S. Ratanaphan, R. Sarochawikasit, N. Kumanuvon, S. Hayakawa, H. Beladi, G. S. Rohrer, T. Okita, Atomistic simulations of grain boundary energies in an austenitic TWIP steel, J. Mater. Sci. 54 (2019) 5570–5583.
[28] G.S. Rohrer, V. Randle, C.-S. Kim, Y. Hu, Changes in the five-parameter grain boundary character distribution in α-brass brought about by iterative thermomechanical processing, Acta Mater. 54 (2006) 4489–4502.
[29] V. Randle, M. Coleman, M. Waterton, The role of $\sum 9$ boundaries in grain boundary engineering, Metall. Mater. Trans. A 42 (2011) 582–586.
[30] M. Laleh, A.E. Hughes, M.Y. Tan, G.S. Rohrer, S. Primig, N. Haghdadi, Grain boundary character distribution in an additively manufactured austenitic stainless steel, Scr. Mater. 192 (2021) 115–119.
[31] H. Beladi, V. Tari, G.S. Rohrer, On $\sum 9$ grain boundary plane orientation, Materialia 25 (2022), 101540.
[32] D.L. Olmsted, S.M. Foiles, E.A. Holm, Survey of computed grain boundary properties in face-centered cubic metals: I. Grain boundary energy, Acta Mater. 57 (2009) 3694–3703.
[33] N. Gokon, M. Kajihara, Experimental determination of boundary energies of $\sum 9$ [110] asymmetric tilt boundaries in Cu, Mater. Sci. Eng. A 477 (2008) 121–128.
[34] K.L. Merkle, D. Wolf, Low energy configurations of symmetric and asymmetric tilt grain boundaries, Philos. Mag. A 65 (1992) 513–530.